AIAA JOURNAL
Vol. 45, No. 3, March 2007

Flow Visualization of Dragonfly Hovering via an Electromechanical Model

Yuan Lu,* Gong Xin Shen,† and Wen Han Su‡
Beijing University of Aeronautics and Astronautics, 100083 Beijing, People's Republic of China

DOI: 10.2514/1.22088

Here, the first physical images revealing the integral flow structures and their evolutions of dragonfly hovering are presented, based on the dye flow visualization conducted on an electromechanical model in water tunnel. Together with the quantitative information derived from the images, several findings were obtained: 1) spanwise flow was conspicuous regardless of the large aspect ratio of the wing; 2) the leading-edge vortex contained dual-vortex structure: the primary vortex did not develop along the leading edge but moved inboard, leaving a space for the formation of a same-sense minor vortex outside the primary vortex; 3) the development of the leading-edge vortex showed a delay with respect to the translational motion of the wing; and 4) in most cases with forewing–hindwing interaction, the interaction was generally detrimental to the leading-edge vortices and was attenuated with the increase of the wing-root spacing.

Nomenclature

AR	=	aspect ratio, R/c
c	=	mean chord length
d	=	wing-root spacing
n	=	stroke frequency
R	=	wing length
r	=	effective model wing length
T	=	stroke period
t	=	time
U_t	=	mean wing-tip translational speed
α	=	angle of attack
β	=	stroke plane angle
γ	=	phase advance of the hindwing
ΔTr	=	rotational duration
φ	=	instantaneous translational angle
ν	=	kinematic viscosity
ρ	=	instantaneous rotational angle
Φ	=	stroke amplitude

Introduction

WHEREAS dragonflies' superior flight qualities (long-time glide, hovering, and agile maneuverability), unique morphological features (filmy wings with large aspect ratio and slender body), as well as the distinctive flapping kinematics (variable phase relations between the fore- and hindwings, highly inclined flapping plane, and relatively small stroke amplitude) have attracted researchers for a long period, the questions on the flight mechanisms, especially the forewing–hindwing interaction, are still open.

Because the calculations based on the steady-state aerodynamics indicated that quasi-steady lift was not adequate to support the insect's weight [1,2], research has focused on the unsteady mechanisms, especially the forewing–hindwing (FW–HW) interaction. Saharon and Luttges [3–5] built a mechanical model simulating the flapping motion of dragonfly and carried out a series of smoke flow visualizations, yet the kinematic simulation quality two decades ago might affect the quality of the flowfields generated by the model. Based on the 2-D numerical simulation, Lan and Sun [6,7] stated unexpectedly that the FW–HW interaction effect was not remarkable and was even detrimental. Later they extended the work to the 3-D and obtained similar results [8]. On the other hand, smoke-wire visualization was conducted on vivid dragonfly and the topological theory was employed in the qualitative analyses [9]. The author pointed out that spanwise flow was not a conspicuous feature of the flowfields. Nevertheless, probably due to the flight condition used (forward flight) and the inherent deficiency of the technique that is hard to discern the flows out of the smoke plane, their conclusions might be not applicable to all situations. Also in the field of experiment, electromechanical model equipped with digital particle image velocimetry (DPIV) technique was used to measure the flowfields at the midspan section [10]. However, in this study, horizontal stroke plane, rather than inclined stroke plane that could generate distinctive flows in down- and upstrokes, was considered [8].

Despite the fact that the sectional visualization in the aforementioned studies has indeed shed some light on the flight mechanisms and forewing–hindwing interactions of dragonflies, only can the global visualization uncover the 3-D structures of the complex flows. In this paper, we present the first physical images that reveal the integral flow structures and their evolutions of dragonfly hovering, based on the dye flow visualization conducted on an electromechanical model in a water tunnel. Three representative hovering modes, that is, 1) counter stroking, 2) in-phase stroking, and 3) hindwing leads 1/4 period, were considered. The quality of the kinematics simulation was also validated. This work serves as the basis and reference for the following in-depth quantitative investigations such as DPIV and force measurements.

Experimental Methods

Model Wings

Aeschna juncea was the typical dragonfly considered (Fig. 1). Based on the data obtained by Norberg [11], the forewing length $R(\mathrm{FW}) = 47.4$ mm and chord length $c(\mathrm{FW}) = 8.1$ mm, rendering the aspect ratio $\mathrm{AR(FW)} = 5.85$; the hindwing length $R(\mathrm{HW}) = 46.0$ mm and chord length $c(\mathrm{HW}) = 11.2$ mm, thus $\mathrm{AR(HW)} = 4.11$.

Reynolds number $Re = U_t c/\nu = 2\Phi nRc/\nu$[12] was the chief similarity parameter considered to guarantee the experimental flowfields similar to the actual ones. $Re(\mathrm{FW}) = 1844$ and $Re(\mathrm{HW}) = 2473$ in actual dragonfly hovering flight, respectively. The model wing planforms were simplified as shown in Fig. 2. To reveal the essence of the FW–HW interaction without the interference of the geometrical factors (e.g., the wing area and the curving leading edge, etc.), the two ipsilateral model wings were

Received 28 December 2005; accepted for publication 18 December 2006.

*Graduate Student, Institute of Fluid Mechanics.
†Professor, Institute of Fluid Mechanics; gx_shen05@yahoo.com.cn.
‡Professor, Institute of Fluid Mechanics.

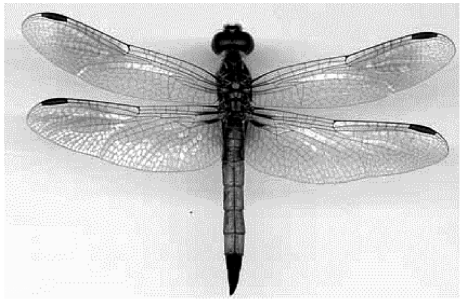

Fig. 1 Dragonfly *Aeschna juncea*.

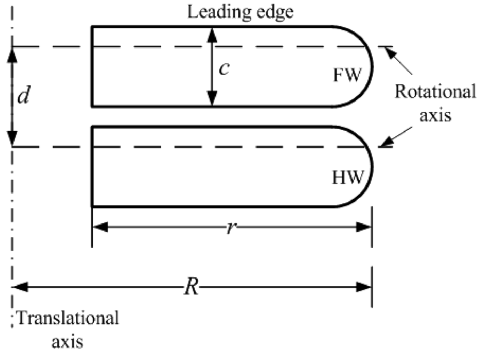

Fig. 2 Simplified model wing planforms.

made identical, with the same aspect as the dragonfly's FW. In experiment, stroke frequency n was set to 0.1 Hz ($n = 36$ Hz in the real hovering condition) [1] to make the flow structures easy to discern. R and c were set to 210 and 36 mm, respectively, resulting in model's $Re = 1569$ [roughly 85% (FW) and 63% (HW) of the real condition]. The difference of Reynolds number between experimental and real flight condition might be troublesome to the similarity of the flowfields. However, prior studies [12–14] suggested that the flows around a flapping wing should not be sensitive to Reynolds number when the Reynolds number reaches the level of 1000.

Each model wing was 3 mm thick and was hollow in structure: both outside layers were fabricated from a 1 mm acrylic sheet to form the wing planform and allowed sufficient strength and rigidity, between which was a cavity that installed a set of dye tubes with diameters of 1 mm. To eliminate the effect of the blunt edges, both of the outer wing surfaces had 45 deg bevels. In addition, the part near the wing root was cut (making the effective wing length $r = 150$ mm and effective AR $= 4.2$) and the minimal wing-root spacing d was set to $1.25c$ to avoid mechanical interference.

Kinematics

The stroke plane deviation was not taken into account and thus there were 2 degrees of freedom for each wing: translation and rotation. *Translation* is the orientative rotation of the wing about the translational axis that is through the wing root (O or o) and vertical to the stroke plane F (defined by O and the minimum and maximum angular locations of the rotational axis y). *Rotation* is the supinating/pronating rotation about y (at 1/4 wing chord from the leading edge [11].) Basically, there are three rotational modes defined by the timing with respect to the translation: 1) advanced, 2) symmetrical, and 3) delayed rotations [15]. Only symmetrical rotation was applied in this study.

Coordinate system is shown in Fig. 3. $OXYZ$ is the inertial orthogonal frame relative to the ground, with X and Y axes in the horizontal plane H. $oxyz$ is the wing-fixed orthogonal frame, with x axis parallel to the wing chord and y axis along the rotational axis. P is a plane parallel to the wing chord and perpendicular to the wing surface, used to define angle of attack. The thick solid line with a filled dot (denotes the leading edge) represents the section of the

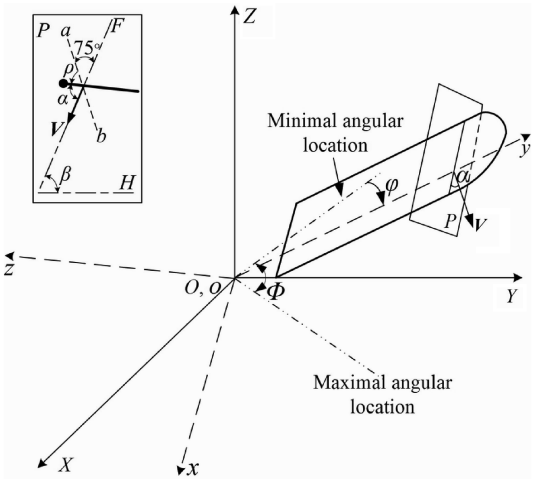

Fig. 3 Coordinate system.

wing. F is the stroke plane. The stroke plane angle β and stroke amplitude Φ are both 60 deg for dragonfly [16]. The instantaneous translational angle φ (begins at the minimum angular location) varies as the cosine function [8,17], thus the translational function is

$$\varphi = 0.5\Phi[1 - \cos(2\pi t/T)] \tag{1}$$

The instantaneous rotational angle ρ (starts from the maximal rotational speed location ab to the wing surface) varies as the simple harmonic function when the wing is rotating, but remains constant when the wing is purely translating. The rotational function is

$$\rho = \begin{cases} \pi/4\sin(\pi t/\Delta T_r) & 0 \le t < 0.2T \\ \pi/4 & 0.2T \le t < 0.3T \\ \pi/4\cos[\pi(t-0.3T)/\Delta T_r] & 0.3T \le t < 0.7T \\ -\pi/4 & 0.7T \le t < 0.8T \\ -\pi/4\cos[\pi(t-0.8T)/\Delta T_r] & 0.8T \le t < T \end{cases} \tag{2}$$

The rotational duration ΔTr was set to $0.4T$ [8]. The midstroke angles of attack were 60 and 30 deg in down- and upstrokes, respectively. The relation between translation and rotation is shown in Fig. 4.

There are mainly three FW–HW phase relationships employed by dragonfly during hovering: 1) counterstroking (CS), used in common hovering; 2) in-phase stroking (IPS), employed chiefly in takeoff; and 3) HW leads 1/4 period (HL1/4), used in maneuvers such as escape [18]. These relationships are differentiated by the phase advance of the HW γ (equal to 180, 0, and 90 deg for counterstroking, in-phase stroking, and HW leads 1/4 period, respectively). The translational function of the HW is

$$\varphi = 0.5\Phi[1 - \cos(2\pi t/T + \gamma)] \tag{3}$$

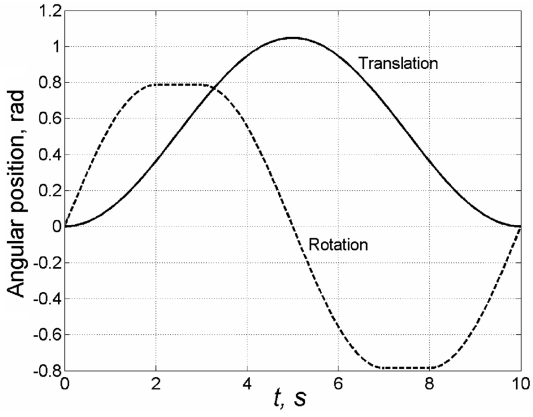

Fig. 4 Translational and rotational curves over one period.

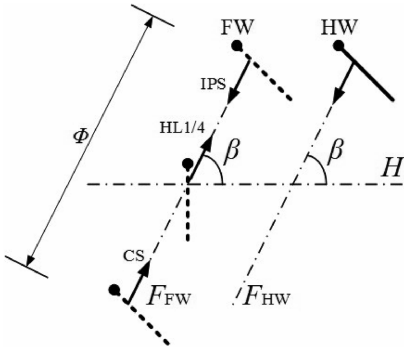

Fig. 5 Forewing–hindwing phase patterns.

Fig. 5 shows the differences of the three FW–HW patterns with the initial positions of the FW and HW.

Kinematics Simulation System

The kinematics simulation system included two identical mechanical systems positioned as the right-lateral wings configuration of the dragonfly and was mounted on the top of the water tunnel. Each of them has 2 degrees of freedom (translation and rotation) driven by two servo motors (Maxon Corp., Sachseln, Switzerland) connected to a controller (Nyquist Corp., Eindhoven, Holland) commanded by the self-written software and output the given motions after corresponding data were discretized and input into the personal computer.

Because in all hovering modes the HW leads the FW [19], only the modification of the FW kinematics was required to realize the FW–HW phase relations. Actually, the absolute values of the input data of the CS and IPS are identical, so merely adjusting the initial position and the sign of the input data of the FW is required. The kinematics simulation was validated based on the comparison between the ideal curves and the output data (data sampling began at $0.1T$). The validations of the CS (or IPS) and HL1/4 are labeled V1 and V2, respectively. In each case, two groups of discretized data (discretization of 100 and 250) were investigaed. In all cases, the output translational motions were almost identical to the ideal curves [see Fig. 6; because the software can only record the original output data of the motors, the y axis in each subgraph is the motor-based angular positions (1.33×10^4 corresponds to 1 deg in this sense). Solid line: translation; dashed line: rotation; solid line with circles: output data]. In V1, 250 divisions was better and was applied (Figs. 6a and 6b); in V2, the two discretizations were only of slight difference and 100 divisions was applied (Figs. 6c and 6d). However, in V2, rotational positional angle could not reach the desired value right after initiating from the rest due to the parameter limitation of the motors. The problem was solved after manually resetting the initial angular position to compensate the deficient angle (roughly 8 deg).

Flow Visualization and Image Sampling

Both vortex [leading-edge vortex (LEV), trailing-edge vortex (TEV), and wing-tip vortex (WTV)] sheet and LEV core (LC) were visualized. Vortex sheet was visualized via the dyes seeping from the narrow gaps (roughly 0.2 mm wide) located on each wing edge; LC was visualized through the dyes released from a single tube placed at the node of each leading edge. The experiment was conducted in the water tunnel in Beijing University of Aeronautics and Astronautics (BUAA), with a test section of $1 \times 1 \times 1.2$ m. No power was input to satisfy the hovering condition. One CCD camera (1008×1018 pixels, Red Lake, San Diego, California) with a lens (Nikon, Tokyo) and with two spotlights were used for image recording (sampling rate was set to five frames per second). The sampling procedures were conducted after the wings had moved for four periods from startup to ensure the flowfield to be fully established. During each sampling, four sequent periods (40 s) were recorded, and the procedures were repeated for five times in separate time for each case. The overall experimental setup is shown in Fig. 7 (Figs. 7a and 7b are side view and top view, respectively; C1, C2: dye

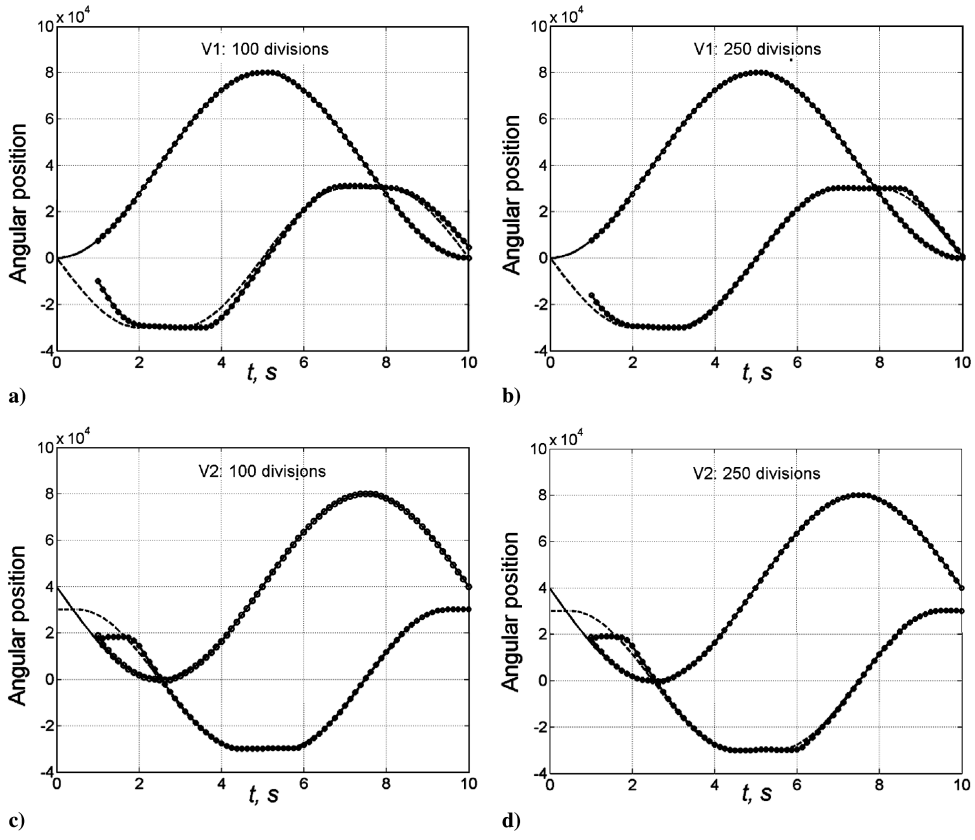

Fig. 6 Validation of the kinematics simulation.

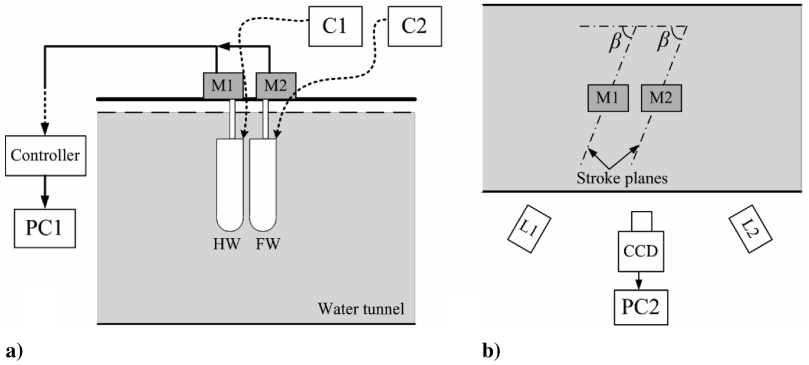

Fig. 7 Experimental setup.

containers; L1, L2: spotlights; M1, M2: mechanical systems; PC1, PC2: personal computers).

Results and Analyses

Single-Wing Case

To investigate the flow characteristics of large-aspect-ratio wing as well as to set a reference for the more complicated FW–HW situations, the case of single wing was studied at first. For convenience, we stipulate the leeward surface of the wing in downstroke or the windward surface in upstroke to be the upper wing surface, and vice versa. The related data of the LC were measured from every frame in one cycle.

LEV Evolution

Figures 8 and 9 show, respectively, the time sequence of the LEV sheet and LC evolutions at the same representative instants. Big white and gray arrows denote the down- and upstroke motions, respectively.

At every beginning of downstroke, a small cylindrical LEV sheet (diameter of about $0.2c$) with no spanwise flow rolled up to the upper wing surface (Figs. 8a and 9a). Accompanying the appearance of the spanwise flow at $0.04T$, the diameter of the LEV rapidly increased to half-chord length, but still kept a cylindrical pattern (Fig. 8b). In this stage, the overall spatial structure of the LEV was basically 2-D.

With the acceleration of the wing, a pressure gradient (denoted with PG+) pointing from the wing root to the wing tip was also increasing, motivating the appearance and development of the spanwise flow. The intensive spanwise flow exhibited in our study conflicts with the results of a recent smoke visualization of forward flight of a dragonfly [9], which stated that the spanwise flow was not conspicuous in the LEV. It is possible that the spanwise flow might be eliminated by the interaction of the bilateral wings, particularly in the case that the LEVs on the bilateral wings combine with each other above the thorax. Nevertheless, in forward flight, the separation of incoming streams behind the blunt head of the animal may be responsible for the interaction of the bilateral LEVs. Yet it is not that case in hovering because the translational speed near the wing bases is close to zero and a large vortex is not likely to be induced. In fact, the LEV with strong spanwise flow has already been well known in

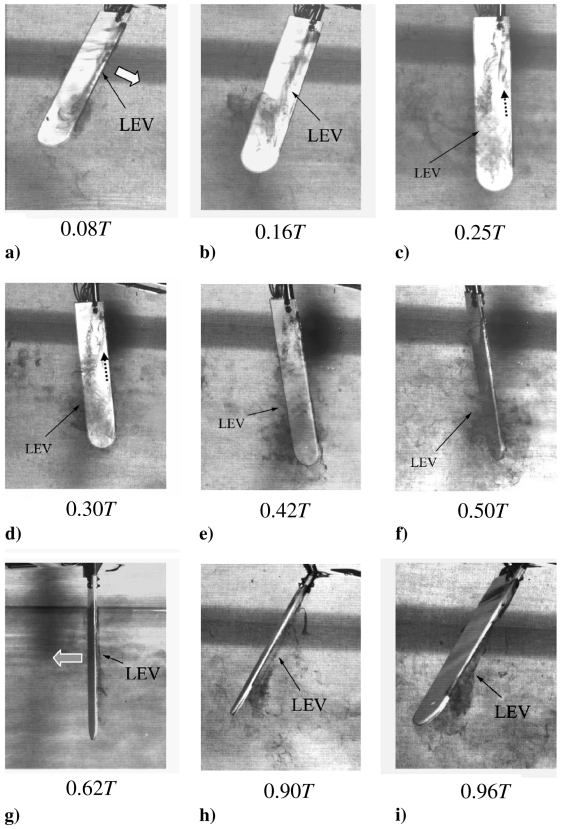

Fig. 8 Evolution of the LEV sheet.

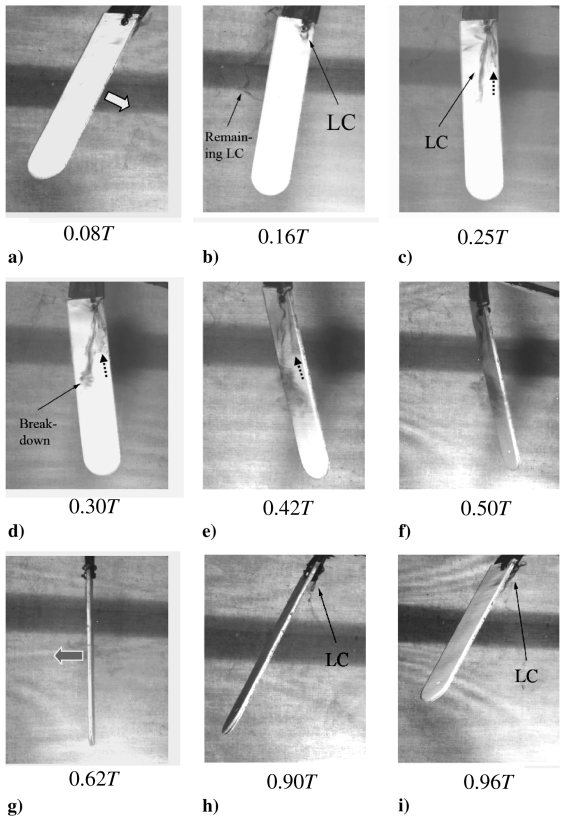

Fig. 9 Evolution of the LEV core.

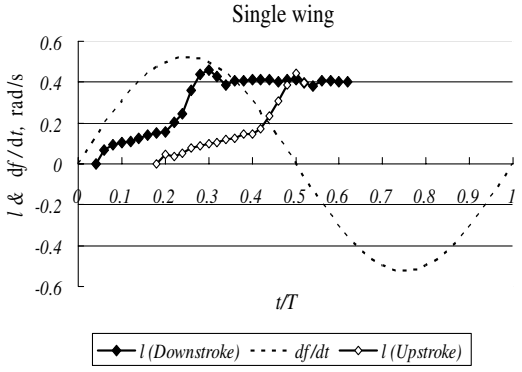

Fig. 10 LC length vs stroke cycle.

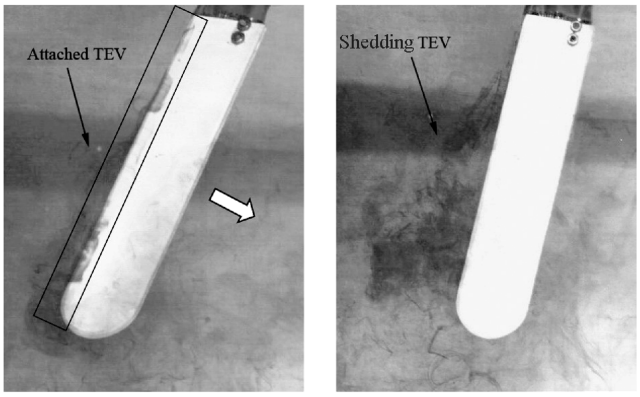

Fig. 11 Trailing-edge vortex in downstroke.

the hovering experiment conducted by Ellington et al. [12], whose mechanical flapper included two bilateral wings.

Back to the issue of LEV evolution, it is unexpected that the LC moved inboard toward the trailing edge (Figs. 9c and 9d), much different from the previous studies of insects with small aspect ratio (such as hawkmoth and fruitfly), which demonstrated that the LEV axes were close to and along the leading edge [12,13]. No prior study of dragonfly has ever reported this phenomenon. Moreover, a minor vortex (denoted with dashed-line arrows in Figs. 8c, 8d, 9c, and 9d) was detected outboard the primary vortex, but it was significantly weaker and shorter than the primary vortex. Such a dual LEV structure resembles that confirmed on a low-sweep delta wing [20], and has been reported in the smoke-wire visualization of butterfly *V. atalanta* [21]. Whereas the rotational sense of this minor vortex was observed consistent with the primary vortex, DPIV validation is required and will be conducted in our following works. In this stage, the LEV transformed to a conical pattern and was 3-D in structure (Figs. 8c–8e). Thomas et al. [9] reported a cylindrical LEV with a constant diameter along the vortex axis. Again, we reckon that such an LEV pattern in [9] should be attributed to the forward-flight condition as suggested by Wang [19].

The diameter of the LEV continued to increase and LC was moving toward the wing tip with a greater speed regardless of the deceleration of the wing, showing a delay with respect to the translational motion of the wing (see Fig. 10: l is defined in Table 1; the curves of the down- and upstroke are put together just for the convenience of comparison, but not indicating that the two LCs appeared and developed at the same time), corresponding to the nonlinear nature of the unsteady flowfield. Nevertheless, vortex breakdown (occurred at $0.30T$, see Fig. 9d) was inevitable due to the decrease of the PG+ as well as the raise of the opposite pressure gradient (PG−, induced by the greater flow speed on the upper wing surface whenever the wing had a positive angle of attack). During this period, the axial speed of LEV was about half of the average wing-tip speed (see Table 1).

During supination, the LEV was getting looser (Figs. 8e and 8f) and the breakdown of the LC was intensified (Figs. 9e and 9f). l dropped from the maximum of 0.46 to 0.38 within $0.04T$ and kept a stable value of about 0.41 until the vortex totally broke down.

During upstroke, the remaining downstroke LEV encountered the leading edge and was "cut" into two parts: one passed through the leading edge and shed from the lower surface of the wing, the other was directly away from the trailing edge on the upper surface. New LEV also formed (Figs. 8g–8i), with the spanwise flow appearing in a later time (at $0.18T$ after the wing began to upstroke); the LEV burst only when the wing began to pronate, and it shed from the trailing edge with a concentrated LC when the wing was downstroking (see the "remaining LC" in Fig. 9b; the curve of upstroke in Fig. 10 was plotted when the LEV still remained on the lower wing surface). Compared with the downstroke, both the rotational speed and diameter of this LEV were smaller, considering the smaller angle of attack in upstroke. LC deviation was also salient, making only the part close to the leading-edge root visible (Fig. 9i).

TEV Evolution

Immediately when the wing began downstroking, a separated shear layer rolled up onto the upper surface of the wing and formed the TEV. The TEV was 2-D and was a cylindrical shape. Then only having stayed on the upper surface for $0.08T$, the TEV shed from the trailing edge (Fig. 11). The case in upstroke was similar.

WTV Evolution

The WTV formed in each down- and upstroke with the similar pattern. Taking the phenomena in downstroke, for example, a separated shear layer at the wing tip rolled up onto the upper surface of the wing immediately after the wing started up. Attaching on the upper wing surface for roughly the same time ($0.08T$) as TEV, the WTV moved toward the trailing edge and shed (see the dashed-line arrow in the middle image in Fig. 12). In the later stage of downstroke, it spiraled (clockwise, see the right image in Fig. 12) away from the wing surface with a "tornado" pattern.

Table 1 Related data of LC in downstroke in various cases

Items	Cases						
	Single wing	CS		IPS		HL1/4	
		FW	HW	FW	HW	FW	HW
Appearing time t_a [a]	0.04	0.08	0.04	0.04	0.2	0.08	0.02
Intact-keeping time t_i [b]	0.26	0.24	0.34	0.22	——	0.27	——
Sustaining time t_s [c]	0.58	0.48	0.52	0.58	0.28	0.78	0.32
Maximal LC length l_{max} [d]	0.46	0.39	0.63	0.33	0.38	0.46	0.34
LEV average axial speed v_a [e]	0.56	0.50	0.58	0.48	0.42	0.42	0.33

[a] $t_a = T_a/T$; T_a was timed from the initiation of downstroke.
[b] $t_i = T_i/T$; T_i is the interval between t_a and the instant when the LEV began breakdown. In the case of IPS and HL1/4, the values of HW were not given for the LEVs collapsed without showing obvious burst.
[c] $t_s = T_s/T$; T_s is the interval between t_a and the instant when the LEV lastly remained concentrated.
[d] $l = L/r$; L was measured from the leading-edge root to the end of LC (or the bursting point when breakdown occurred).
[e] $v_a = V_a/V_t$; $V_a = L_{max}/T_i$, $V_t = 48$ mm/s.

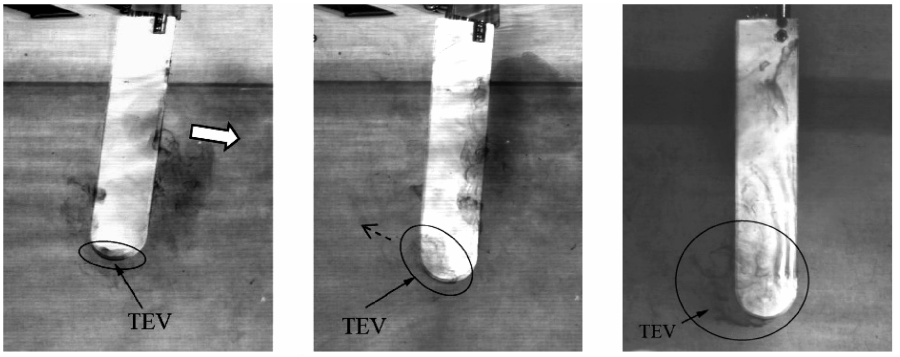

t=0.08T t=0.20T t=0.34T

Fig. 12 Wing-tip vortex in downstroke.

Cases with FW–HW Interaction

In these cases, during upstrokes no noticeable concentrated LEV was detected due to the remarkable decrease in the effective angle of attack caused by the strong downwash in the wakes. The flow phenomena in downstrokes were diversified in different FW–HW interactions, and thus were concentrated in this study. In addition, the flowfields were difficult to discern owing to the turbulentlike dyed flows and the contaminated background water, hence the evolutionary behaviors of the LC were the central flow structures in investigation, and qualitative data were derived from the flow images.

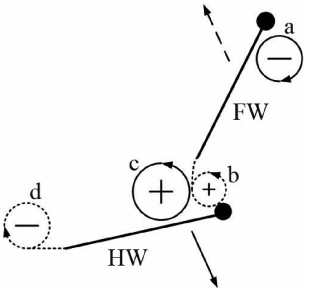

Fig. 14 Supposed flow interaction.

Counterstroking

When the FW was downstroking (HW in upstroke), the LEV on the FW evolved with almost the same pattern as the single-wing case. Nevertheless, its $l_{\max}$, v_a, t_i, and t_s were 88, 89, 92, and 83% of the single-wing case, respectively (Table 1), suggesting that the FW–HW interaction did not take strong influence on the FW, but such an influence was detrimental.

When the HW was downstroking (FW in upstroke), $l_{\max}$, t_i of HW's LC are 37 and 31% larger than the single-wing case, respectively, indicating that HW's LEV was reinforced by the FW–HW interaction. Two facets could be responsible for this reinforcement: 1) when the two wings were moving close to each other, the accelerating FW quickened the incoming stream of the HW, and thus enhanced the circulation of HW's LEV; and 2) although the FW moved away from the HW after then, its wakes with the same-sign vorticity encountered and reinforced HW's LEV. This can be further demonstrated from Fig. 13 that when FW's wakes were captured by HW's leading edge, they induced remarkable vorticity on the HW (see the arrow in Fig. 13b). This wing–wake interaction is illustrated in Fig. 14 (a, c are LEVs on the FW and HW, respectively; b, d are TEVs shed from the FW and HW, respectively.) The numerical simulation in [8] shows that the vertical force was larger on the HW than on the FW and ascribed that to the larger area of the HW. However, according to the previous analyses and note the identical FW and HW planforms in our study, the FW–HW interaction can be a qualified candidate responsible for the force discrepancy of the ipsilateral wings.

In addition, when the two wings were moving close to each other, HW's LC was bent remarkably (see the bent dashed line in Fig. 15d). Though it cannot be used to elucidate the property of the FW–HW interaction, this phenomenon is also an evidence demonstrating the existence of the FW–HW interference. Also, the dual-vortex structures were observed on both FW and HW (see the dashed-line arrows in Figs. 15a, 15c, and 15d). Unlike the single-wing case or the

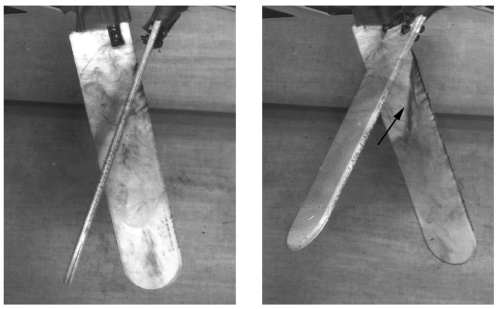

t=0.38T t=0.48T

a) b)

Fig. 13 LEV on the HW was reinforced by the FW's wakes.

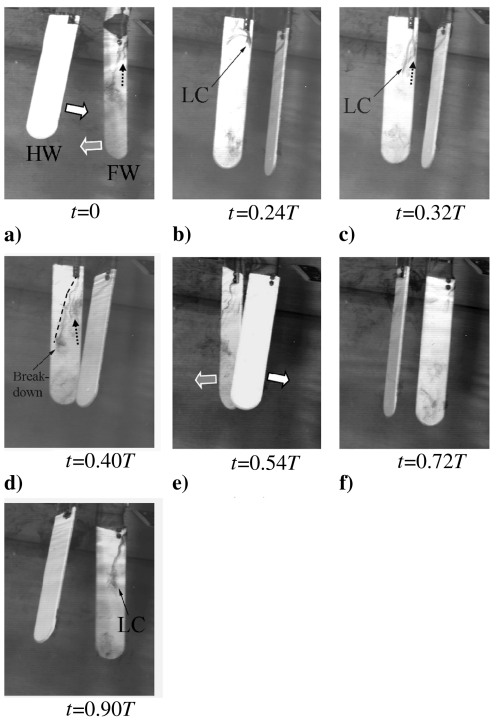

t=0 t=0.24T t=0.32T

a) b) c)

t=0.40T t=0.54T t=0.72T

d) e) f)

t=0.90T

g)

Fig. 15 LC evolution in the counterstroking.

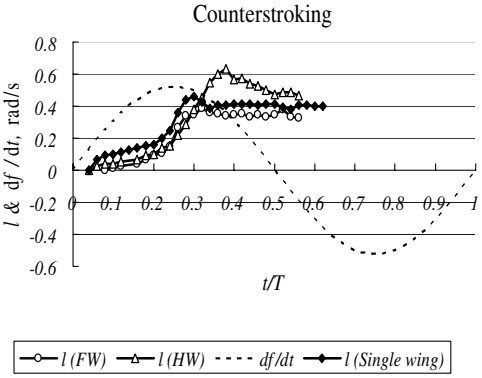

Fig. 16 LC length vs stroke cycle in downstroke.

situation on the FW, LEV on the HW shed directly from the trailing edge. From Fig. 16 (the curves of the FW and HW are put together just for the convenience of comparison, but not indicating the two LCs appeared and developed at the same time; the curve of the single-wing case is also presented for comparison), the general trend was similar, but the delay effect in this case was more dramatic than in the single-wing case.

In-Phase Stroking

During downstroke, HW's LC not only developed with a small v_a (25% less than the single-wing case), but was also much weaker than the FW counterpart (Figs. 17d and 17e). Actually, HW's LEV directly broke down as a whole, with the shortest sustaining time in all cases (only 48% of the single-wing case). Obviously, HW's LEV was impaired by the FW–HW interaction. As a matter of fact, HW's LEV was consistently offset by FW's wake that was with the opposite-sign vorticity, because the two tandem wings were close to each other throughout the cycles (illustrated in Fig. 18, the vortices are labeled with the same fashion as in Fig. 14). Previous 2-D computational study has obtained similar results [6].

On the other hand, after keeping intact for $0.22T$ (85% of the single-wing case), FW's LEV broke down (Fig. 17d). The presence

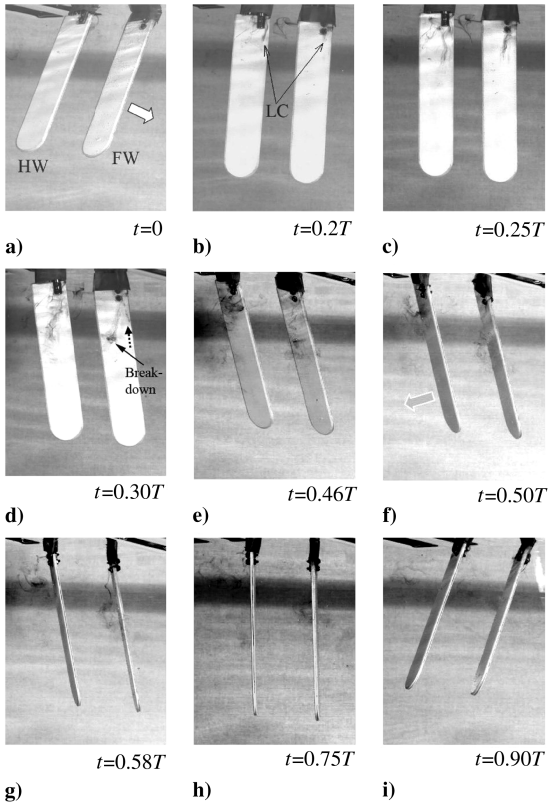

Fig. 17 LC evolution in the in-phase stroking.

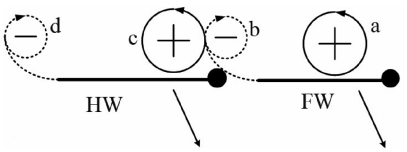

Fig. 18 Supposed flow interaction.

of HW may deflect the incoming stream and cause a decrease in FW's effective angle of attack, and thus the circulation of FW's LEV. Nevertheless, FW's LEV survived a considerable long time ($0.58T$, the same as the single-wing case). Figure 19 further illustrates this phenomena; again, the curves of the FW and HW are put together only for the convenience of comparison, but not indicating the two LCs appeared and developed at the same time. Generally, though weaker than the single-wing case, FW's LEV was more stable than the HW counterpart, suggesting again that HW suffered more from the FW–HW interaction. Additionally, the dual LEV was observed on FW (see the dashed-line arrow in Fig. 17d).

HW Leads 1/4 *Period*

HW's LC became feeble (Fig. 20c) after $0.25T$. Similar to the case on the HW in IPS, HW's LC directly broke down as a whole (Figs. 20c–20e), and its v_a was the smallest in all cases (0.33, only

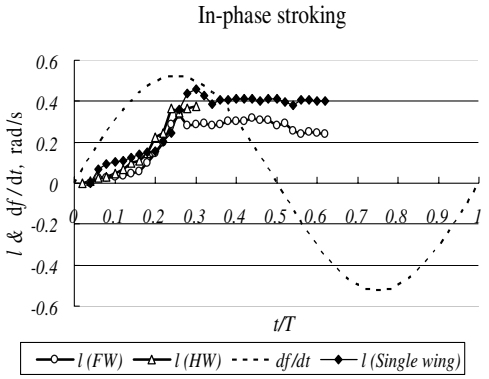

Fig. 19 LC length vs stroke cycle in downstroke.

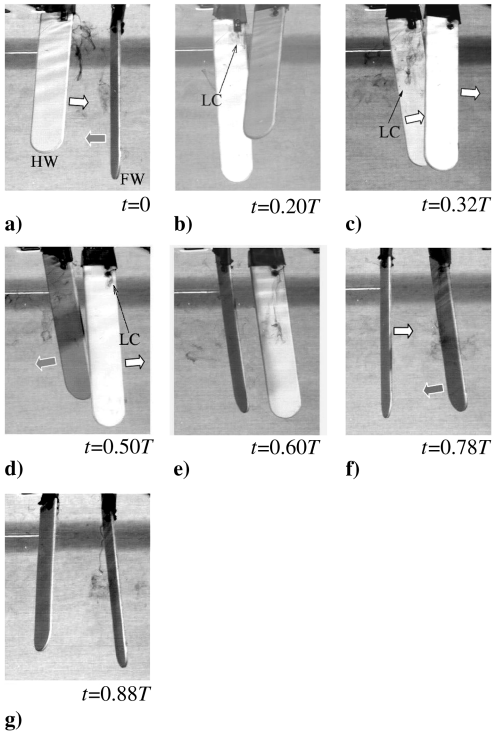

Fig. 20 LC evolution in the hindwing leads 1/4 period.

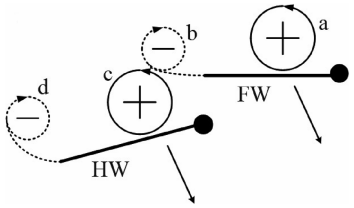

Fig. 21 Supposed flow interaction.

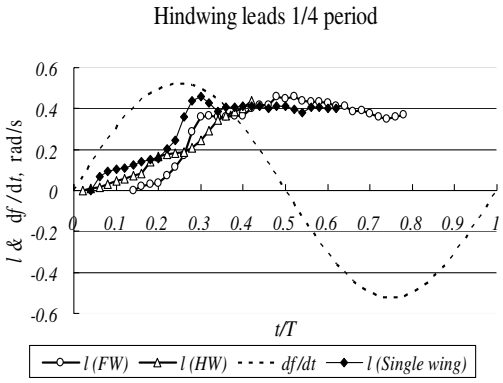

Fig. 22 LC length vs stroke cycle in downstroke.

59% of the single-wing case.) Before $0.25T$, the upstroking FW sped up the incoming flow of HW and thus contributed positively to its LEV. However, because the two wings were close to each other, FW's TEV (with an opposite vorticity sign) reached the HW within a short time and shadowed HW's LEV all through the stroke (illustrated in Fig. 21). This detrimental influence of FW's TEV exceeded the previous positive contribution of the FW, resulting in the total effect disadvantageous to HW's LEV. Contrary, Maybury and Lehmann [10] pointed out that HW's LEV could successfully escape from FW's wakes. However, it is possible that the different kinematic patterns employed in our and their experiments could explain the discrepancies of the results. For instance, in our study, the TEV that shed from the FW with a 60 deg midstroke angle of attack during downstroke should be stronger and impact a larger region than in their experiment, in which the midstroke angle of attack was 45 deg in both up- and downstrokes.

On the other hand, FW's LC developed with a similar pattern as in the single-wing case, but did not show evident retrogression after breaking down. Moreover, it even kept moving toward the wing tip until the FW completed the downstroke (Fig. 22; the curves of the FW and HW are put together just for the convenience of comparison, but not indicating the two LCs appeared and developed in the same time), resulting in the greatest sustaining time in our records ($t_s = 0.78$, 134% of the single-wing case). Therefore, the LEV on the FW was reinforced, but the influential pattern was not clear. In addition, the delay effect was more dramatic than the single-wing case (Fig. 22).

In this case, dual LEV was unnoticeable.

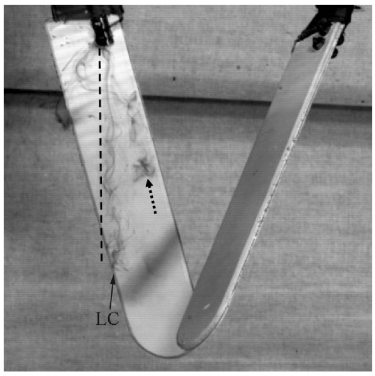

Fig. 23 Wing-root spacing d was increased to $3.25c$.

Effect of Wing-Root Spacing

CS was the typical pattern considered. The bend of HW's LC vanished when the wing-root spacing d was enlarged to $3.25c$ (see the straight dashed line in Fig. 23.) It is until the wing-root spacing was increased to $5.25c$ that the condition on HW became identical to the single-wing case, consistent with the result of [10]. Therefore, the flow interaction between the two tandem wings diminished with the increase of the wing-root spacing, obeying the asymptotic nature of the vorticity field [22]. And again, the dual-LEV structure was observed (see the dashed-line arrow in Fig. 23).

Conclusions

In this experimental study, spanwise flow was dramatic on the large-aspect-ratio wing in flapping motion. Nevertheless, the LEV with spanwise flow did not develop along the leading edge but moved inboard, leaving a space for the formation of another minor vortex outboard the primary vortex, which resembles the dual LEV structure on nonslender delta wing. In most cases, the primary LEV cores evolved with the similar pattern: before breaking down, they spiraled out toward the wing tip even when the wing was decelerating, showing a delay with respect to the translational motion of the wing, then retrogressed within a short time to a stable level until totally broken down. In the situations with FW–HW interaction, concentrated LEV was remarkable only during downstrokes, suggesting that downstroke should be, to large extent, responsible for the lift production as indicated in the prior computational works. Except the situations on the HW in the CS and on the FW in the HL1/4, LEVs in other two-wing cases were weaker than the case of single wing, demonstrating that the FW–HW interaction is generally detrimental to the LEVs (lift production).

Acknowledgments

This work is supported by Chinese Natural Scientific Foundation CNSF10472011. The authors express their appreciation to Mao Sun for the valuable suggestions, and the anonymous reviewers for their important comments on the manuscript.

References

[1] Norberg, R. A., "Hovering Flight of the Dragonfly *Aeschna Juncea L.*, Kinematics and Aerodynamics," *Swimming and Flying in Nature*, edited by T. Y. Wu, C. J. Brokaw, and C. Brennen, Plenum Press, New York, 1975, pp. 763–781.

[2] Somps, C., and Luttges, M., "Dragonfly Flight: Novel Uses of Unsteady Separation Flow," *Science*, Vol. 228, No. 14, 1985, pp. 1326–1328.

[3] Saharon, D., and Luttges, M. W., "Three-Dimensional Flow Produced by a Pitching-Plunging Model Dragonfly Wing," AIAA Paper 87-0121, 1987, pp. 1–17.

[4] Saharon, D., and Luttges, M. W., "Visualization of Unsteady Separated Flow Produced by Mechanically Driven Dragonfly Wing Kinematics Model," AIAA Paper 88-0569, 1988, pp. 1–23.

[5] Saharon, D., and Luttges, M. W., "Dragonfly Unsteady Aerodynamics: The Role of the Wing Phase Relations in Controlling the Produced Flows," AIAA Paper 89-0832, 1989, pp. 1–19.

[6] Lan, S. L., and Sun, M., "Aerodynamic Force and Flow Structures of Two Airfoils in Flapping Motions," *Acta Mechanica Sinica*, Vol. 17, Nov. 2001, pp. 310–331.

[7] Lan, S. L., and Sun, M., "Aerodynamic Interactions of Two Airfoils in Unsteady Motion," *Acta Mechanica*, Vol. 150, 2001, pp. 39–51.

[8] Sun, M., and Lan, S. L., "A Computational Study of the Aerodynamic Forces and Power Requirements of Dragonfly (*Aeshna Juncea*) Hovering," *Journal of Experimental Biology*, Vol. 207, 2004, pp. 1887–1901.

[9] Thomas, A. L. R., Taylor, G. K., Srygley, R. B., Nudds, R. L., and Bomphrey, R. J., "Dragonfly Flight: Free-Flight and Tethered Flow Visualizations Reveal a Diverse Array of Unsteady Lift-Generating Mechanisms, Controlled Primarily via Angle of Attack," *Journal of Experimental Biology*, Vol. 207, 2004, pp. 4299–4323.

[10] Maybury, W. J., and Lehmann, F.-O., "The Fluid Dynamics of Flight Control by Kinematic Phase Lag Variation Between Two Robotic Insect Wings," *Journal of Experimental Biology*, Vol. 207, 2004, pp. 4707–4726.

[11] Norberg, R. A., "The Pterostigma of Insect Wings an Inertial Regulator

of Wing Pitch," *Journal of Comparative Physiology*, Vol. 81, 1972, pp. 9–22.
[12] Ellington, C. P., van den Berg, C., Willmott, A. P., and Thomas, A. L. R., "Leading-Edge Vortices in Insect Flight," *Nature*, Vol. 384, Dec. 1996, pp. 626–630.
[13] Birch, J. M., Dickson, W. B., and Dickinson, M. H., "Force Production and Flow Structure of the Leading Edge Vortex on Flapping Wings at High and Low Reynolds Numbers," *Journal of Experimental Biology*, Vol. 207, 2004, pp. 1063–1072.
[14] Wu, J. H., and Sun, M., "Unsteady Aerodynamic Forces of a Flapping Wing," *Journal of Experimental Biology*, Vol. 207, 2004, pp. 1137–1150.
[15] Ellington, C. P., "The Aerodynamics of Hovering Insect Flight. 3. Kinematics," *Philosophical Transactions of the Royal Society of London Series B, Biological Sciences*, Vol. 305, 1984, pp. 41–78.
[16] Ellington, C. P., "The Aerodynamics of Hovering Insect Flight. 6. Lift and Power Requirements," *Philosophical Transactions of the Royal Society of London Series B, Biological Sciences*, Vol. 305, 1984, pp. 41–78.
[17] Wakeling, J. M., and Ellington, C. P., "Dragonfly Flight 2. Velocities, Accelerations and Kinematics of Flapping Flight," *Journal of Experimental Biology*, Vol. 200, 1997, pp. 557–582.
[18] Alexander, D. E., "Unusual Phase Relationships Between the Forewings and Hindwings in Flying Dragonflies," *Journal of Experimental Biology*, Vol. 109, 1984, pp. 379–383.
[19] Wang, Z. J., "Dissecting Insect Flight," *Annual Review of Fluid Mechanics*, Vol. 37, 2005, pp. 183–210.
[20] Taylor, G. S., Schnorbus, T., and Gursul, I., "An Investigation of Vortex Flows over Low Sweep Delta Wings," AIAA Paper 2003-4021, June 2003.
[21] Srygley, R. B., and Thomas, A. L. R., "Unconventional Lift-Generating Mechanisms in Free-Flying Butterflies," *Nature*, Vol. 420, Dec. 2002, pp. 660–664.
[22] Wu, J. C., "Theory for Aerodynamic Force and Moment in Viscous Flows," *AIAA Journal*, Vol. 19, April 1981, pp. 432–441.

M. Auweter-Kurtz
Associate Editor